The charging mechanism of Li_2MnO_3

Niccoló Guerrini[ꝑ], Liyu Jin[ꝑ], Juan G. Lozano[†], Kun Luo[†], Adam Sobkowiak, Kazuki Tsuruta[‡], Felix Massel[§], Laurent-Claudius Duda[§], Matthew R. Roberts[ꝑ] and Peter G. Bruce[*,†].

[†]Departments of Materials and Chemistry, University of Oxford, Parks Road, Oxford OX1 3PH, United Kingdom

[‡]Japan Synchrotron Radiation Research Institute (JASRI), 1-1-1 Kouto, Sayo, Hyogo 679-5198, Japan

[§]Department of Physics and Astronomy, Division of Molecular and Condensed Matter Physics, Uppsala University, Box 516, S-751 20 Uppsala, Sweden

″Etteplan Sweden AB, SE-171-54 Solna, Sweden

[ꝑ]Dyson Technology Ltd., Tetbury hill, Malmesbury, SN16 0RP, United Kingdom

ABSTRACT: Operando mass spectroscopy demonstrates quantitatively that lithium extraction from Li_2MnO_3 is charge compensated by oxygen loss (O-loss) not oxidation of oxide ions which are retained within the structural framework (O-redox). This data is confirmed by X-ray absorption and emission spectroscopy. Li NMR shows that the two-phase core-shell structure, which forms on charging, is composed of an intact Li_2MnO_3 core and highly disordered shell containing no Li, with a composition close to MnO_2. Discharge involves Li insertion into the disordered shell. CO_2 and O_2 are detected on charging at 15 mAg^{-1}, whereas charging by GITT forms only CO_2; an observation in agreement with the previously described model of oxygen evolution from high voltage cathodes producing singlet O_2 that reacts with the electrolyte forming CO_2. The dominance of oxygen evolution over O-redox is in accord with the model of O-loss occurring when the oxide ions are undercoordinated; O in the shell devoid of Li is coordinate by only 2 Mn.

Introduction

Recognition that it is possible to oxidise the O^{2-} ions in lithium rich transition metal oxides has spurred significant interest in this process as a means of increasing the energy storage of cathodes for lithium-ion batteries.[1–5] When this happens, two processes are well known to occur: loss of oxygen (O-loss) from the lattice in an irreversible process or O^{2-}-oxidation/reduction (O-redox), meaning oxidation of lattice ions which are retained within the structural framework and can be reduced back to O^{2-} on discharge. Most O-active compounds exhibit both oxygen loss and O-redox. Li_2MnO_3 ($Li[Li_{1/3}Mn_{2/3}]O_2$ using the layered notation) is among the simplest of Li-rich compounds. Early studies suggested that charge compensation for Li_2MnO_3 was associated with proton intercalation or oxidation of Mn beyond 4+.[6–8] More recent works have shown that Mn does not participate in transition metal charge compensation[9] and calculations have shown that redox activity on the oxygen centres compensates for the extraction of Li ions[10–13].

Here we use a combination of operando mass spectrometry, hard and soft X-ray spectroscopy, NMR and STEM, to quantify the amount of charge compensation due to O-loss *vs.* O-redox. We show quantitatively that only O-loss occurs. [6]Li NMR and STEM demonstrate that a core-shell structure is formed on O-loss involving complete de-lithiation in the shell and no change in the core, which remains as pristine Li_2MnO_3. We also differentiate between O-loss that results in CO_2 formation and O lost directly as O_2, the former occurring in the first stage of charging. The large quantity of CO_2 that is generated permits investigation of the hypothesis that some of the CO_2 may arise from oxidation of Li_2CO_3 on the surfaces of the particles. Our results show that the dominant source of CO_2 arises from O extracted from the lattice that then reacts with electrolyte, not Li_2CO_3.

Experimental

Synthesis: Li_2MnO_3 was synthesized using a sol−gel method[14]. Stoichiometric amounts of $LiCH_3COO \cdot 2H_2O$ (99.0%, Sigma-Aldrich), and $Mn(CH_3COO)_2 \cdot 4H_2O$ (99.0%, Fluka) were dissolved in distilled water containing 0.1 mol of resorcinol (99.0%, Fluka), 0.15 mol of formaldehyde (Fluka 36.5% in water), and 0.25 mmol of Li_2CO_3 (99.0%, Sigma-Aldrich). The mixture was heated under vigorous stirring at 70 °C until an opaque uniform gel was formed. The gel was dried at 90 °C overnight, and finally heated in air first at 500 °C for 12 h and then at 800 °C for 12 h to obtain the final product.

ICP-OES: Elemental analysis of the as-prepared sample was carried out after its complete dissolution in acidic solution by ion coupled plasma optical emission spectroscopy (ICP-OES) using a PerkinElmer Optima 7300DV ICP-OES. This allowed for the exact quantification of Li and Mn.

Powder X-ray Diffraction (XRD): Powder X-ray diffraction analysis was carried out using a Rigaku SmartLab X-ray powder diffractometer equipped with a 3 kW Cu anode.

Soft X-ray Absorption and Resonant Inelastic X-ray Spectroscopy: SXAS and RIXS spectra were recorded at beamline BL27SU of the RIKEN/JASRI Spring8 synchrotron in Japan. Ex situ cathode samples were loaded onto adhesive copper tape and measured under 10^{-6} Pa high-vacuum conditions. To obtain SXAS spectra at the O K-edge and Mn L-edge, partial fluorescence yield (PFY) method was employed and the fluorescence signal was recorded using silicon drift detectors (SSD). The O K-edge RIXS spectra were recorded using an XES monochromator composed of a varied-line-spacing cylindrical grating and a CCD detector with a resolution of 0.5 eV in the energy range of interest.

Electrochemical Measurements: The working electrodes were prepared with a composition of 80 wt % active material, 10 wt % Super P carbon, and 10 wt % polytetrafluoroethylene (PTFE) binder. The components were combined with a pestle and mortar and then calendared to ~60 μm between two sheets of Al foil before being punched into 10 mm $\varnothing$ pellets. The pellets were assembled into coin cells with a Li metal counter electrode and LP30 as electrolyte (Sigma Aldrich,1 M solution of $LiPF_6$ in 1:1 wt % mixture of EC:DMC). Electrochemical measurements were carried out using a Biologic VMP3 potentiostat.

Operando Electrochemical Mass Spectrometry: Operando mass spectrometry analysis was performed to detect the gases generated during electrochemical cycling. The operando mass spectrometry system was built in-house and employed a commercial quadrupole mass spectrometer (Thermo Fischer) with a turbomolecular pump (Pfeiffer Vacuum). The setup employed was based on a previously described design.[15] The operando mass spectrometry cell consisted of a lithium metal anode disk, electrolyte (1 M $LiPF_6$ in PC), and a cathode disk composed of 80 wt % active material, 10 wt % Super P carbon, and 10 wt % polytetrafluoroethylene (PTFE) binder. Calibration and quantification methods were as described in detail elsewhere [16].

MAS-NMR: Solid-state nuclear magnetic resonance (NMR) experiments were performed in a 3.2 mm probe-head on a 400 MHz Bruker Avance HD III spectrometer at the ^6Li Larmor frequency of 58.9 MHz. Magic angle spinning (MAS) of 20 kHz was applied. The spectra were recorded with rotor-synchronised Hahn-echo pulse sequence; the applied π/2 pulse length and the delay between π/2 and π pulses were 3.5 μs and 44.8 μs. The MAS probe-head temperature was controlled at 268 K (the real sample temperature in the rotor was about 298 K during spinning at 20 kHz). Due to the paramagnetism of the samples, all electrode samples were mixed/diluted with dried MgO powder with a weight ratio about 1:3 (1-part sample) before packed in rotors in an Ar-filled glovebox. The ^6Li spectra were externally referenced with 1 M LiCl aqueous solution at 0.0 ppm. The Li_2MnO_3 containing 100% ^7Li ($^7Li_2MnO_3$) was synthesized using the same sol-gel route as described except the lithium was sourced from $^7LiOH \cdot H_2O$ (Sigma-Aldrich 99.9%), which was dissolved in a water solution of acetic acid to obtain the ^7Li-acetate aqueous solution.

TGA-MS: Thermogravimetric Analysis was carried out on powder sample of ~20 mg under inert Ar atmosphere using a NETZSCH Jupiter STA 449 F3 TGA. This was coupled with a NETZSCH Aëolos QMS 403 D mass spectrometer to provide operando mass spec.

Scanning Transmission Electron Microscopy: ADF-STEM and ABF-STEM data were collected on an aberration corrected JEOL ARM 200F operated at 200 kV. The convergence semi-angle used was 22 mrad, and the collection semi-angles were 9.5-20.7 mrad (ABF) and 69.6-164.8 mrad (ADF). In all cases, sets of fast-acquisition multi-frame images were recorded and subsequently corrected for drift and scan distortions using SmartAlign.4
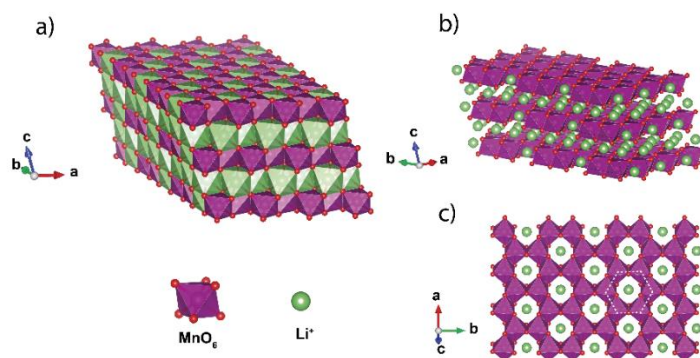

Figure 1: Structure of Li_2MnO_3 (a), the cubic close packed O3 structure of Li_2MnO_3; (b) visualised along the b axis showing the stacking sequence of $Li_{1/3}Mn_{2/3}$ and lithium layers; (c) in plane honeycomb ordering within the TM-layer.

Results and Discussion

Li_2MnO_3 was synthesised as described in the method section. Powder X-ray diffraction, Fig. S1, confirmed formation of Li_2MnO_3, the structure of which is composed of cubic close packed O^{2-} ions between which alternate layers of Li^+ ions and $[Li^+_{1/3}Mn^{+4}_{2/3}]$ ions in octahedral coordination, Fig 1. The ions in the predominantly transition metal layers form the well-known honeycomb ordering, as described previously.[17–20] The composition was confirmed by ICP-OES. The particle morphology consists of 50-150 nm primary particles agglomerated into secondary particles of approximately 20-50 μm as shown in Fig S2. The charge/discharge curve for Li_2MnO_3 during the Operando Electrochemical Mass-Spec (OEMS) experiment is shown in Fig 2, and is in good accord with data reported previously for Li_2MnO_3[8,21,22]. On charging, the potential rises rapidly to 4.5 V, consistent with negligible $Mn^{3+/4+}$ oxidation. It is clear that gas evolution occurs from the initial charging of the cell and continues throughout.

It has been suggested previously that the CO_2 arising when lithium rich and even stoichiometric lithium intercalation compounds are charged could be associated with the oxidation of Li_2CO_3 present on the surfaces of the particles[23,24]. The large quantity of CO_2 formed on charging Li_2MnO_3, compared with most lithium transition metal compounds, makes Li_2MnO_3 an excellent material with which to test this proposition. To investigate whether, following the synthesis of Li_2MnO_3 at 800 °C in air and cooling, reaction with CO_2 had resulted in Li_2CO_3 formation, TGA-MS (Fig. S4) was employed. Li_2CO_3 starts decomposing at ~ 750 °C[25], therefore the mass loss above this temperature on heating quantifies the amount of Li_2CO_3 present. TGA-MS of Li_2MnO_3 revealed a mass loss of 0.02 mg of Li_2CO_3 per mg of Li_2MnO_3. The oxidation of Li_2CO_3 is described by the following equation[26] :

	E_{rev}/V vs Li
$Li_2CO_3 \rightarrow 2Li^+ + 2e^- + \frac{1}{2}O_2 + CO_2$	3.82
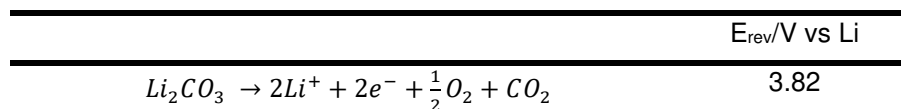
If the amount of Li_2CO_3 was fully oxidised on charging, it would account for 17.5% of the total amount of CO_2 and 10.8% of the total amount of O_2 evolved Table 1 (calculation shown in SI). This leads us to conclude that at least

3

86.5% of the CO_2 and 89.2% of the O_2 evolved on charging Li_2MnO_3 are NOT from oxidation of Li_2CO_3. The results demonstrate that the majority of CO_2 and O_2 formed on charging Li_2MnO_3, arise from O-loss from the lattice and not from Li_2CO_3 oxidation.

To determine quantitatively if oxygen loss from the lattice dominates the charging mechanism, we need to calculate the charge associated with O-loss from the quantity of gases evolved and compare this with the actual charge passed that contributes to oxidation of Li_2MnO_3. Previous studies have described equations for the reaction of oxygen lost from the lattice with the electrolyte forming CO_2 [27–29]. From the stoichiometry of these reactions and correcting for the amount of CO_2 formed directly by oxidation of the small amount of Li_2CO_3 present the amount of charge passed associated with oxygen loss from Li_2MnO_3 that forms CO_2 can be calculated and added to the amount from direct evolution of O_2. The results are presented in Table 1 and show that the charge passed which is not associated with Li_2CO_3 decomposition is associated almost entirely with O-loss from the lattice. Additionally, approximately 1-2% of the gas evolved could be due the electrochemical decomposition of the electrolyte at the cathode surface during charge. This has been demonstrated in our previous work, by performing OEMS on the spinel $LiNi_{0.5}Mn_{1.5}O_4$ material which is known not to lose O from the lattice in the potential window of investigation [30].
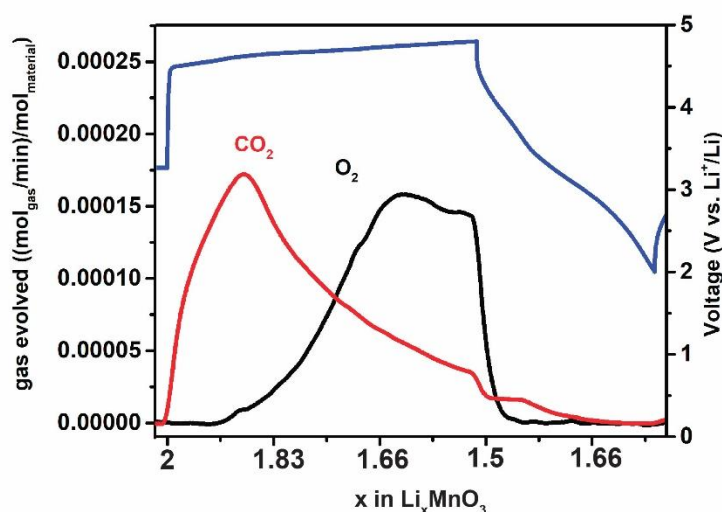

Figure 2: Voltage profile and gas evolution during the first galvanostatic cycle (a). The right and left y-axes represent the electrode potential and total gas release rate respectively. Current density 0.225 mA/cm^2

To investigate directly the evolution of the electronic structure of Li_2MnO_3 during charge and discharge, soft X-ray spectroscopy and resonant inelastic X-ray scattering were employed, Fig 3. The oxygen K edge SXAS pre-edge region between 527 and 536 eV (Fig 3b shaded region) corresponds to the transitions between the O 1s core shell and the O 2p valence shell hybridized with the transition metals 3d orbitals. Its area is sensitive to the presence of hole-state density formed on charging just above the Fermi energy[31,32]. Data were collected at the points shown on the charge/discharge curve in Fig 3c. For the pristine material the two peaks arise from transitions into the empty Mn t_{2g} and e_g states hybridised with the O 2p states and are similar to the spectra observed for MnO_2 (black dots).
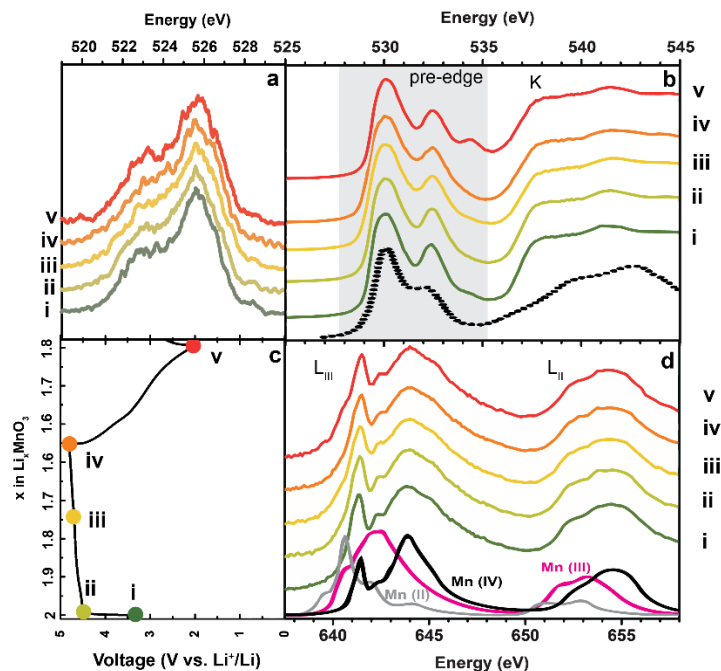
Figure 3: (a) RIXS spectra for Li_2MnO_3 collected with an excitation energy of 531.5 eV at different points along the first charge (spectra i-iv). (b) Soft X-ray Absorption spectra for the oxygen K-edge of Li_2MnO_3 (i-v) and for the reference material MnO_2 (black dotted line). The pre-edge area (527-534 eV) corresponds to the transitions from the oxygen 1s core level to the energy states immediately above the Fermi energy. (d) Soft X-ray Absorption spectra for the manganese L-edge of Li_2MnO_3 (i-v) and for the reference oxidation states Mn(II), Mn(III) and Mn(IV).

The spectra throughout charging show no significant differences from the pristine material in this region, demonstrating that there are no new hole-states formed, consistent with no oxidation of Mn^{4+} and no generation of hole states on the O ions. The presence of a shoulder appearing at 534.5 eV for the discharged sample (spectrum v in Fig 3b) could be associated with the reduction of the electrolyte and consequent deposition of lithium carbonate at the material surface during the lithiation process[33]. RIXS was employed to probe the formation of electron hole-states on O^{2-} (i.e. the presence of reversible redox activity, O-redox, at the oxygen centres). No variation is detected in the RIXS (Fig 3a) spectral weight distribution during charging confirming that no hole-states are formed on the oxygen centres. Additionally, confirmation that Mn^{4+} does not undergo any further oxidation when charging at this potential is seen in the Mn L edge data in Fig 4d. Throughout the electrochemical cycling the spectra remain invariant and exhibit the profile of the standard for Mn^{4+}, also shown in Fig 4d. In summary, spectroscopic data confirm that there is no evidence for oxidation of either Mn^{4+} or O^{2-} generating stable hole-states on charging.

When oxidation of O^{2-} leads to O-loss, transition metal migration towards the bulk fills the Li^+ vacancies generated by Li extraction, leading to densification at the surface. In the case of Li-rich materials such as $Li[Li_{0.2}Ni_{0.2}Mn_{0.6}]O_2$ this leads to a rocksalt/spinel shell (3-4 nm).[34–36]. However, in Li_2MnO_3, O-loss is more severe. Scanning transmission electron microscopy (STEM) was carried out on the Li_2MnO_3 particles in order to explore whether a similar rocksalt phase forms. A STEM image of Li_2MnO_3 charged to 4.8V was collected (Fig. 4) showing the formation of a surface layer (~6 nm) that appears to be highly disordered (enlargement in Fig. 4) rather than the crystalline rocksalt shell observed in other Li-rich materials. To probe this further and to rule out the possibility that the shell is present in the pristine material, high resolution STEM images were collected for the pristine and charged particles, Fig 5b and 5c. In both cases in the bulk it is possible to observe a layered structure with the characteristic 'dumbbell' arrangement for the oxygen atoms, and the disordered layer appears only in the charged sample.
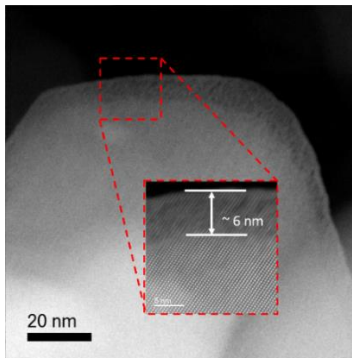
Figure 4: STEM image of a particle of Li_2MnO_3 charged to 4.8 V vs. Li/Li^+ along the [100] direction. The shell had an average thickness of ~6 nm. Current density 0.225 mA/cm^2

Given the highly disordered nature of the shell, [6]Li NMR was employed to further characterise the structure. The spectra for the pristine, charged and the discharged material are shown in Figure 5. The NMR shifts corresponding to Li in the alkaline metal and transition metal layers are highlighted with shading in the pristine spectrum, the remaining peaks being spinning side bands. On charging to 4.8 V, there is no noticeable change in the shape of the spectra compared with that of the pristine. The only significant change is the reduced mass-normalised intensities of the two Li environments. This is consistent with the electrode de-lithiating via a 2-phase reaction forming a core-shell structure, the new phase completely lithium deficient and the original phase. The latter, whilst diminished in quantity shows no further changes. Such behaviour is in accord with the voltage plateau on charge.
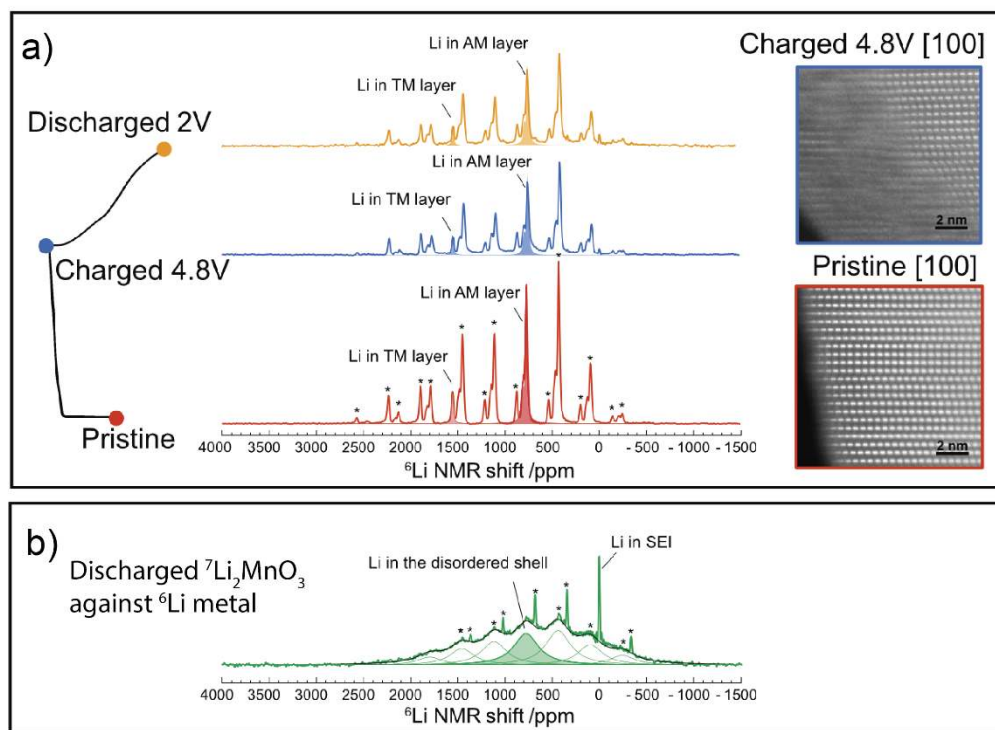

Figure 5: a) [6]Li NMR spectra showing the pristine Li_2MnO_3 (red), charged to 4.8V (blue), subsequent discharge to 2V (yellow). On the pristine spectrum, the isotropic alkaline metal (AM) Li and transition metal (TM) Li environments are highlighted and all other peaks are spinning sidebands which are starred (MAS rate is 20kHz). The STEM images of [100] orientation show the atomic structures at the particle edge in the pristine and charged states. b) Spectrum of discharged [7]Li_2MnO_3 cycled vs. [6]Li metal. All the spectra are normalized against sample mass except the one of [7]Li_2MnO_3. The Spectrum is fitted (black line in 5b) and deconvoluted and the isotropic shift is highlighted in green. The sharp peak at 0 ppm indicates a diamagnetic Li environment and is likely from Li in SEI layer on the surface from electrolyte decomposition.

On discharge, the spectrum (yellow, Fig. 5a) shows a small amount of line-broadening but significantly, the reinserted Li does not result in an obvious increase of the spectral intensity. One explanation is that the reinserted Li

6

resides in the structurally disordered shell created upon charging and their NMR shifts are so broad that they merge with the baseline when plotted against the high intensity peaks from highly crystalline "pristine" environments. To test this, an electrode with 100% ^7Li was synthesized and a single charge and discharge against a ^6Li metal anode was performed. The ^6Li spectrum of this discharged sample shows only the shifts of reinserted Li, as ^7Li nuclei do not resonate near the ^6Li frequency. The spectrum (green Fig. 5b) shows a very broad peak in accord with reinserted Li being located in the disordered shell and a very sharp peak at 0 ppm shift corresponding to Li into electrolyte decomposition products. Several sidebands for Li in the SEI are also present in the spectrum and marked with a star. The spectral deconvolution reveals a broad peak centred around 772 ppm. This shift is in accord with Li in alkali metal layers and its broad linewidth comes from an ensemble of structurally similar Li shifts, suggesting that the inserted Li reside in alkali-metal-layer-like environments that are disordered by stacking faults and other defects, which is consistent with the direct observation from STEM. Broad NMR peaks associated with the disordered environments of the shell, similar to the ones showed in Fig. 5b, could be convoluted within the spectrum for the discharged Li_2MnO_3 presented in Fig. 5a (yellow) but their intensity would be too low to be detected due to the strong NMR signal associated with Li contained in the crystalline core of the particles. Combining the information from the STEM images and ^6Li NMR spectra, it is clear that a disordered shell is formed on charging to 4.8 V that is devoid of lithium and lithium is reinserted into it during the discharge, i.e. the shell is electrochemically active, while the core remains as pristine-like and electrochemically inactive throughout.

The dominance of O-loss in Li_2MnO_3 is in accord with previous observations that O-loss often occurs where the oxide ions in Li-rich cathodes can become severely undercoordinated by loss of coordinating Li^+ ions [37]. In the case of Li_2MnO_3, every O^{2-} ion is coordinated by 2 Mn^{4+} ions located in the transition metal layer (TM) and 4 Li^+ ions of which 1 is located in the TM layer and 3 in the alkali metal layer (AM), $(Mn_2Li)_{TM}-O-(Li_3)_{AM}$. On charging, oxidation of O^{2-} weakens the metal-oxygen bonds and as Li^+ is mobile the Li^+ coordinating the oxide ions are readily lost leading to oxidised oxide ions that are severely undercoordinated, $(Mn_2)_{TM}-O$. The undercoordinated oxygens are unstable favouring O-loss from the lattice leaving a densified manganese oxide shell. This differs from Li-Rich materials such as $Li_{1.2}Co_{0.13}Ni_{0.13}Mn_{0.54}O_2$. In Li_2MnO_3 ($Li[Li_{1/3}Mn_{2/3}]O_2$), all the oxygens are coordinated by 4 Li and 2 Mn (OLi_4Mn_2). As Ni and Co are substituted in the in Li_2MnO_3 lattice some of the Li are replaced by transition metals, i.e. now not all the O are coordinated 4 Li. While some O will still be OMn_2Li_4, others will be for example OMn_2NiLi_3, no Li in the TM layer. This reduces the number of undercoordinated oxygens relative to the total number of oxygens leading to a decrease in the degree of oxygen loss (O-loss) and to an increase in stable oxidised oxide ions (O-redox) which remain within the structural framework as observed in previous work.[32]

~0.45 Li are extracted on charge (Fig. 2). Of these, 0.06 Li are associated with Li_2CO_3 decomposition. Given that the amorphous shell is devoid of Li and the core consists of pristine Li_2MnO_3, the volume ratio of shell to core corrected for the presence of Li_2CO_3 is expected to be approximately 1:5, i.e. the shell should account for ~20% of the particle volume. The STEM images indicated a shell thickness of approx. ~6 nm, Fig 4. With an average particle size of 100 nm and assuming a simple spherical particle morphology the shell volume is expected to be ~22%, in good agreement with the 20% predicted value. Since all of the O-loss is from the shell, we can estimate a shell composition of MnO_2.

One point to be addressed regards the origin of the evolved gasses. Are there two mechanisms of oxygen evolution from the lattice, one that leads to O_2 and the other CO_2? Jung et al[38] has already shown that singlet O_2 is evolved on charging Li rich and even stoichiometric cathodes. This reactive species attacks the electrolyte forming CO_2. Jung proposes that whether CO_2 or O_2 is observed depends on the rate of singlet O_2 evolution vs the rate of reaction with the electrolyte; on charging, CO_2 is observed first as fresh electrolyte is readily available at the electrode/electrolyte interface, then, as the electrolyte adjacent to the cathode particles is consumed, further singlet O_2 cannot react with the electrolyte, it is therefore quenched to the stable triplet state appearing as O_2 gas in OEMS at later stages if charging. To investigate whether appearance of CO_2 during the first stage of charging Li_2MnO_3 with O_2 at the latter stage is due to a similar process, OEMS was carried out on an electrode that was charged with a galvanostatic intermittent titration technique (GITT). A constant current of 15 mAg^{-1} was applied over a 10-minute period, followed by 30 minutes at OCV. The main difference between GITT and galvanostatic charge is in the

timescale of the two techniques. The OCV period in the GITT should allow fresh electrolyte to diffuse to the electrode surface before further singlet O_2 release, i.e. all singlet O_2 reacts with the electrolyte with CO_2 as main gaseous by-product. This does not happen in the galvanostatic charge where the supply of electrolyte which has not already reacted with singlet O_2 is limited, i.e. the singlet O_2 self-quenching mechanism is favoured with O_2 as main by-product at high states of charge. The GITT result, Figure 6, show negligible O_2 gas, only CO_2, in accord with the dominant oxygen evolution being singlet O_2 which reacts with the electrolyte to generate CO_2.[28] The trace for CO_2 rises soon after the first pulse and does not completely return to background levels between each pulse, indicating a relatively large time delay for all the gas to be removed from the cell. The CO_2 trace was integrated to evaluate the charge associated with its evolution, following the procedure described above. The results are reported in Table 1, where again correction for the 2% by mass of Li_2CO_3 has been made. The results yield a predicted charge passed from CO_2 of approximately 144 mAhg^{-1} which compares well with the electrochemical charge passed of ~145 mAhg^{-1}.

Table 1 Comparison of the charge accounted for by CO_2 and O_2 loss with the electrochemical performance in the GITT and Galvanostatic regime. In both cases the CO_2 and O_2 evolved were corrected for the quantity formed by oxidation of Li_2CO_3. A more detailed version of the table is presented in SI.

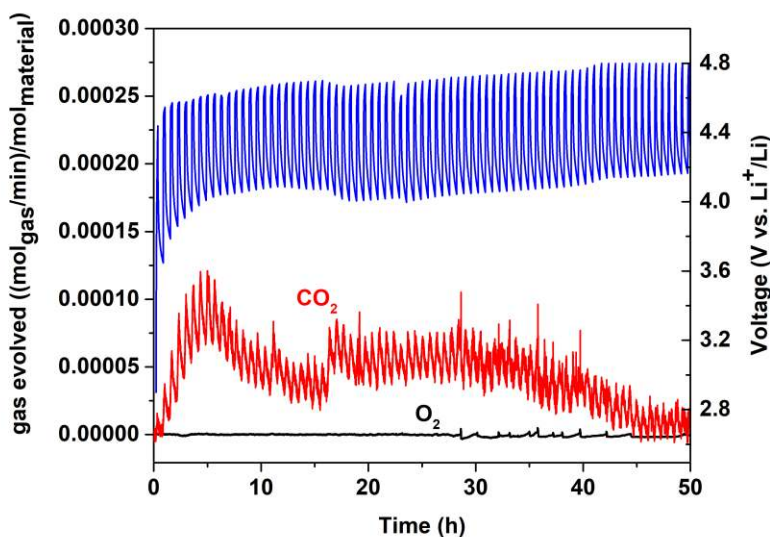| Charging Regime	Total charge passed (mAhg^{-1})	Charge passed minus charge associated with Li_2CO_3 oxidation (mAhg^{-1})	Total Charge determined from gas loss (mAhg^{-1})	Total Charge determined from gas loss corrected for Li_2CO_3 contribution (mAhg^{-1})
Galvanostatic	102	87.5	99.5	85
GITT	145	130.5	144	129.5

Figure 6 Operando electrochemical mass spectrometry for Li_2MnO_3 charged with a galvanostatic intermittent titration protocol, in figure are reported the galvanostatic titration charge (blue line), the oxygen trace (black line), the carbon dioxide trace (red line). The right y-axis represents the electrode potential while the left y-axis the gas release rate expressed as moles of gas per minute per mole of active material. Current density 0.225 mA/cm^2

Conclusions

We show by quantifying the gas evolved on charging that the charge compensation mechanism in Li_2MnO_3 is dominated by oxygen loss from the lattice, in good agreement with previous findings from DFT calculations[11–13,39].

The two-phase charging process results in the formation of a fully de-lithiated and highly disordered shell of composition MnO_2 and pristine (ordered) Li_2MnO_3 core as observed by NMR and STEM analyses. Discharge involves reinsertion for Li into the disordered shell. The dominance of O-loss as the charging mechanism is in accord with the previously described model of O-loss occurring when the O-ions are severely under-coordinated, in this case OMn_2Li_4 in Li_2MnO_3 becomes OMn_2 in the shell on charging. Additionally, it has been shown that very little of the CO_2 observed here is from surface carbonate species. The balance of CO_2 to O_2 observed on charge depends on the charging rate, which fits well with the model described in previous works, in which evolved O_2 reacts with the electrolyte to form CO_2 until electrolyte starvation near the cathode particles surface inhibits this reaction leading to direct observation of O_2 gas.

References

(1)   Sathiya, M.; Rousse, G.; Ramesha, K.; Laisa, C. P.; Vezin, H.; Sougrati, M. T.; Doublet, M. L.; Foix, D.; Gonbeau, D.; Walker, W.; et al. Reversible Anionic Redox Chemistry in High-Capacity Layered-Oxide Electrodes. *Nat. Mater.* **2013**, *12* (9), 827–835. https://doi.org/10.1038/nmat3699.

(2)   McCalla, E.; Abakumov, A. M.; Saubanere, M.; Foix, D.; Berg, E. J.; Rousse, G.; Doublet, M.-L.; Gonbeau, D.; Novak, P.; Van Tendeloo, G.; et al. Visualization of O-O Peroxo-like Dimers in High-Capacity Layered Oxides for Li-Ion Batteries. *Science (80-.).* **2015**, *350* (6267), 1516–1521. https://doi.org/10.1126/science.aac8260.

(3)   Lu, Z.; Dahn, J. R. Understanding the Anomalous Capacity of $Li/Li[Ni_xLi_{(1/3-2x/3)}Mn_{(2/3-x/3)}]O_2$ Cells Using In Situ X-Ray Diffraction and Electrochemical Studies. *J. Electrochem. Soc.* **2002**, *149* (7), A815. https://doi.org/10.1149/1.1480014.

(4)   Zheng, J. M.; Li, J.; Zhang, Z. R.; Guo, X. J.; Yang, Y. The Effects of TiO_2 Coating on the Electrochemical Performance of $Li[Li_{0.2}Mn_{0.54}Ni_{0.13}Co_{0.13}]O_2$ Cathode Material for Lithium-Ion Battery. *Solid State Ionics* **2008**, *179* (27–32), 1794–1799. https://doi.org/10.1016/j.ssi.2008.01.091.

(5)   Seo, D.-H.; Lee, J.; Urban, A.; Malik, R.; Kang, S.; Ceder, G. The Structural and Chemical Origin of the Oxygen Redox Activity in Layered and Cation-Disordered Li-Excess Cathode Materials. *Nat. Chem.* **2016**, *8* (7), 692–697. https://doi.org/10.1038/nchem.2524.

(6)   Robertson, A. D.; Bruce, P. G. Mechanism of Electrochemical Activity in Li_2MnO_3. *Chem. Mater.* **2003**, *15* (10), 1984–1992. https://doi.org/10.1021/cm030047u.

(7)   Kalyani, P.; Chitra, S.; Mohan, T.; Gopukumar, S. Lithium Metal Rechargeable Cells Using Li_2MnO_3 as the Positive Electrode. *J. Power Sources* **1999**, *80* (1–2), 103–106. https://doi.org/10.1016/S0378-7753(99)00066-X.

(8)   Yu, D. Y. W.; Yanagida, K.; Kato, Y.; Nakamura, H. Electrochemical Activities in Li_2MnO_3. *J. Electrochem. Soc.* **2009**, *156* (6), A417. https://doi.org/10.1149/1.3110803.

(9)   Kubobuchi, K.; Mogi, M.; Ikeno, H.; Tanaka, I.; Imai, H.; Mizoguchi, T. Cite As. *Appl. Phys. Lett* **2014**, *104*, 53906. https://doi.org/10.1063/1.4864167.

(10)   Koyama, Y.; Tanaka, I.; Nagao, M.; Kanno, R. First-Principles Study on Lithium Removal

from Li_2MnO_3. *J. Power Sources* **2009**, *189* (1), 798–801. https://doi.org/10.1016/j.jpowsour.2008.07.073.

(11)   Chen, H.; Islam, M. S. Lithium Extraction Mechanism in Li-Rich Li_2MnO_3 Involving Oxygen Hole Formation and Dimerization. *Chem. Mater.* **2016**, *28* (18), 6656–6663. https://doi.org/10.1021/acs.chemmater.6b02870.

(12)   Xiao, R.; Li, H.; Chen, L. Density Functional Investigation on Li_2MnO_3. *Chem. Mater.* **2012**, *24* (21), 4242–4251. https://doi.org/10.1021/cm3027219.

(13)   Koyama, Y.; Tanaka, I.; Nagao, M.; Kanno, R. First-Principles Study on Lithium Removal from Li_2MnO_3. *J. Power Sources* **2009**, *189* (1), 798–801. https://doi.org/10.1016/j.jpowsour.2008.07.073.

(14)   Luo, K.; Roberts, M. R.; Hao, R.; Guerrini, N.; Liberti, E.; Allen, C. S.; Kirkland, A. I.; Bruce, P. G. One-Pot Synthesis of Lithium-Rich Cathode Material with Hierarchical Morphology. *Nano Lett.* **2016**, *16* (12), 7503–7508. https://doi.org/10.1021/acs.nanolett.6b03296.

(15)   Peng, Z.; Freunberger, S. A.; Chen, Y.; Bruce, P. G. A Reversible and Higher-Rate Li-O2battery. *Science (80-.).* **2012**, *337* (6094), 563–566. https://doi.org/10.1126/science.1223985.

(16)   Chen, Y.; Freunberger, S. A.; Peng, Z.; Bardé, F.; Bruce, P. G. Li-O_2 Battery with a Dimethylformamide Electrolyte. *J. Am. Chem. Soc.* **2012**, *134* (18), 7952–7957. https://doi.org/10.1021/ja302178w.

(17)   Boulineau, A.; Croguennec, L.; Delmas, C.; Weill, F. Structure of Li_2MnO_3 with Different Degrees of Defects. *Solid State Ionics* **2010**, *180* (40), 1652–1659. https://doi.org/10.1016/j.ssi.2009.10.020.

(18)   Boulineau, A.; Croguennec, L.; Delmas, C.; Weill, F. Reinvestigation of Li_2MnO_3 Structure: Electron Diffraction and High Resolution TEM. *Chem. Mater.* **2009**, *21* (18), 4216–4222. https://doi.org/10.1021/cm900998n.

(19)   Massarotti, V.; Bini, M.; Capsoni, D.; Altomare, A.; Moliterni, A. G. G. Ab Initio Structure Determination of Li_2MnO_3 from X-Ray Powder Diffraction Data. *J. Appl. Crystallogr.* **1997**, *30* (2), 123–127. https://doi.org/10.1107/S0021889896012460.

(20)   Strobel, P.; Lambert-Andron, B. Crystallographic and Magnetic Structure of Li_2MnO_3. *J. Solid State Chem.* **1988**, *75* (1), 90–98. https://doi.org/10.1016/0022-4596(88)90305-2.

(21)   Rana, J.; Stan, M.; Kloepsch, R.; Li, J.; Schumacher, G.; Welter, E.; Zizak, I.; Banhart, J.; Winter, M. Structural Changes in Li_2MnO_3 Cathode Material for Li-Ion Batteries. *Adv. Energy Mater.* **2014**, *4* (5), 1300998. https://doi.org/10.1002/aenm.201300998.

(22)   Sun, Y.; Zan, L.; Zhang, Y. Enhanced Electrochemical Performances of Li_2MnO_3 Cathode Materials via Adjusting Oxygen Vacancies Content for Lithium-Ion Batteries. *Appl. Surf. Sci.* **2019**, *483*, 270–277. https://doi.org/10.1016/j.apsusc.2019.03.210.

(23)   Renfrew, S. E.; McCloskey, B. D. Residual Lithium Carbonate Predominantly Accounts for First Cycle CO_2 and CO Outgassing of Li-Stoichiometric and Li-Rich Layered Transition-Metal Oxides. *J. Am. Chem. Soc.* **2017**, *139* (49), 17853–17860.

https://doi.org/10.1021/jacs.7b08461.

(24) Armstrong, A. R.; Holzapfel, M.; Novák, P.; Johnson, C. S.; Kang, S.-H.; Thackeray, M. M.; Bruce, P. G. Demonstrating Oxygen Loss and Associated Structural Reorganization in the Lithium Battery Cathode Li [$Ni_{0.2}Li_{0.2}Mn_{0.6}$]O_2. *J. Am. Chem. Soc.* **2006**, *128* (26), 8694–8698. https://doi.org/10.1021/ja062027+.

(25) Kim, J. W.; Lee, H. G. Thermal and Carbothermic Decomposition of Na_2CO_3 and Li_2CO_3. *Metall. Mater. Trans. B Process Metall. Mater. Process. Sci.* **2001**, *32* (1), 17–24. https://doi.org/10.1007/s11663-001-0003-0.

(26) Yang, S.; He, P.; Zhou, H. Exploring the Electrochemical Reaction Mechanism of Carbonate Oxidation in Li–Air/CO_2 Battery through Tracing Missing Oxygen. *Energy Environ. Sci.* **2016**, *9* (5), 1650–1654. https://doi.org/10.1039/C6EE00004E.

(27) Mahne, N.; Renfrew, S. E.; McCloskey, B. D.; Freunberger, S. A. Electrochemical Oxidation of Lithium Carbonate Generates Singlet Oxygen. *Angew. Chemie Int. Ed.* **2018**, *57* (19), 5529–5533. https://doi.org/10.1002/anie.201802277.

(28) Wandt, J.; Freiberg, A. T. S.; Ogrodnik, A.; Gasteiger, H. A. Singlet Oxygen Evolution from Layered Transition Metal Oxide Cathode Materials and Its Implications for Lithium-Ion Batteries. *Mater. Today* **2018**, *21* (8), 825–833. https://doi.org/10.1016/j.mattod.2018.03.037.

(29) Freunberger, S. A.; Chen, Y.; Peng, Z.; Griffin, J. M.; Hardwick, L. J.; Bardé, F.; Novák, P.; Bruce, P. G. Reactions in the Rechargeable Lithium–O_2 Battery with Alkyl Carbonate Electrolytes. *J. Am. Chem. Soc.* **2011**, *133* (20), 8040–8047. https://doi.org/10.1021/ja2021747.

(30) Luo, K.; Roberts, M. R.; Hao, R.; Guerrini, N.; Pickup, D. M.; Liu, Y.-S.; Edström, K.; Guo, J.; Chadwick, A. V.; Duda, L. C.; et al. Charge-Compensation in 3d-Transition-Metal-Oxide Intercalation Cathodes through the Generation of Localized Electron Holes on Oxygen. *Nat. Chem.* **2016**, *8* (7), 684–691. https://doi.org/10.1038/nchem.2471.

(31) Hy, S.; Su, W.-N.; Chen, J.-M.; Hwang, B.-J. Soft X-Ray Absorption Spectroscopic and Raman Studies on $Li_{1.2}Ni_{0.2}Mn_{0.6}O_2$ for Lithium-Ion Batteries. *J. Phys. Chem. C* **2012**, *116* (48), 25242–25247. https://doi.org/10.1021/jp309313m.

(32) Luo, K.; Roberts, M. R.; Guerrini, N.; Tapia-Ruiz, N.; Hao, R.; Massel, F.; Pickup, D. M.; Ramos, S.; Liu, Y.-S.; Guo, J.; et al. Anion Redox Chemistry in the Cobalt Free 3d Transition Metal Oxide Intercalation Electrode Li[$Li_{0.2}Ni_{0.2}Mn_{0.6}$]O_2. *J. Am. Chem. Soc.* **2016**, *138* (35), 11211–11218. https://doi.org/10.1021/jacs.6b05111.

(33) Qiao, R.; Chuang, Y.-D.; Yan, S.; Yang, W. Soft X-Ray Irradiation Effects of Li_2O_2, Li_2CO_3 and Li_2O Revealed by Absorption Spectroscopy. *PLoS One* **2012**, *7* (11), e49182. https://doi.org/10.1371/journal.pone.0049182.

(34) Boulineau, A.; Simonin, L.; Colin, J.-F. F.; Canévet, E.; Daniel, L.; Patoux, S. Evolutions of $Li_{1.2}Mn_{0.61}Ni_{0.18}Mg_{0.01}O_2$ during the Initial Charge/Discharge Cycle Studied by Advanced Electron Microscopy. *Chem. Mater.* **2012**, *24* (18), 3558–3566. https://doi.org/10.1021/cm301140g.

(35) Lu, P.; Yan, P.; Romero, E.; Spoerke, E. D.; Zhang, J. G.; Wang, C. M. Observation of Electron-Beam-Induced Phase Evolution Mimicking the Effect of the Charge-Discharge Cycle in Li-Rich Layered Cathode Materials Used for Li Ion Batteries. *Chem. Mater.* **2015**, *27* (4), 1375–1380. https://doi.org/10.1021/cm5045573.

(36) Lin, F.; Markus, I. M.; Nordlund, D.; Weng, T. C.; Asta, M. D.; Xin, H. L.; Doeff, M. M. Surface Reconstruction and Chemical Evolution of Stoichiometric Layered Cathode Materials for Lithium-Ion Batteries. *Nat. Commun.* **2014**, *5*, 3529. https://doi.org/10.1038/ncomms4529.

(37) Seo, D. H.; Lee, J.; Urban, A.; Malik, R.; Kang, S.; Ceder, G. The Structural and Chemical Origin of the Oxygen Redox Activity in Layered and Cation-Disordered Li-Excess Cathode Materials. *Nat. Chem.* **2016**, *8* (7), 692–697. https://doi.org/10.1038/nchem.2524.

(38) Jung, R.; Metzger, M.; Maglia, F.; Stinner, C.; Gasteiger, H. A. Oxygen Release and Its Effect on the Cycling Stability of $LiNi_xMn_yCo_zO_2$ (NMC) Cathode Materials for Li-Ion Batteries. *J. Electrochem. Soc.* **2017**, *164* (7), A1361–A1377. https://doi.org/10.1149/2.0021707jes.

(39) Cho, E.; Kim, K.; Jung, C.; Seo, S. W.; Min, K.; Lee, H. S.; Park, G. S.; Shin, J. Overview of the Oxygen Behavior in the Degradation of Li_2MnO_3 Cathode Material. *J. Phys. Chem. C* **2017**, *121* (39), 21118–21127. https://doi.org/10.1021/acs.jpcc.7b04937.

Supporting Information

- PXRD
- SEM
- TGA-MS
- Contribution of Li_2CO_3 to the charge and gas loss

Table of Contents graphic